Viewing perspective in energetic neutral atom intensity

Yihua Zheng,[1] Anthony T. Y. Lui,[1] and Mei-Ching Fok[2]

Received 30 January 2008; revised 10 July 2008; accepted 22 July 2008; published 12 September 2008.

[1] Through interspacecraft comparison of energetic neutral oxygen (ENO) intensity from two different vantage points provided by IMAGE and Geotail, Lui et al. (2005) showed that viewing perspective plays a very important role in the observed ENO intensity level during a magnetic storm period. Motivated by the findings of Lui et al. (2005), we investigate how viewing perspective influences energetic neutral atom emissions from a modeling perspective. The main results of this paper are that (1) our simulation results, based upon O^+ ion fluxes from the Comprehensive Ring Current Model and the subsequent ENO calculation, reproduce the total differential ENO intensity obtained from two spacecraft to a reasonable degree and (2) further analysis of our results indicates that pitch angle anisotropy in ring current ion flux, a crucial physical quantity in ring current dynamics, is one major contributor to the difference in energetic neutral atom intensity from different viewing perspectives.

Citation: Zheng, Y., A. T. Y. Lui, and M.-C. Fok (2008), Viewing perspective in energetic neutral atom intensity, *J. Geophys. Res.*, *113*, A09217, doi:10.1029/2008JA013070.

1. Introduction

[2] Energetic neutral atoms (ENA), which are products of charge exchange between singly charged energetic ions and neutrals of the geocorona, enable global imaging of the ring current. ENA emission detection serves as an innovative diagnostic tool for detailed investigations of energetic particles and has contributed greatly to addressing key issues of storm and substorm dynamics. The very first ENA image of the ring current was reported by *Roelof* [1987] using ISEE 1 data. Detection of ENAs was also reported from Geotail [*Lui et al.*, 1996, 2001], Polar [*Henderson et al.*, 1997; *Jorgensen et al.*, 1997], and Astrid [*C:son Brandt et al.*, 2001]. The launch of the IMAGE satellite has provided unprecedented imaging capabilities to help understand the global electrodynamics of the Earth's magnetosphere. The evolution from a compact, asymmetric ring current during the storm main and early recovery phases to an expanded and more symmetric one during the late recovery phase was observed [*Pollock et al.*, 2001]. Using observations of High Energy Neutral Atom (HENA) imager onboard the IMAGE satellite, *Mitchell et al.* [2001] found that the ion injection penetrated more deeply into the magnetosphere ($L \sim 3\ R_E$) during a major storm than that during a small storm. An unexpected feature emerges from the HENA observations. *C:son Brandt et al.* [2002] found that during the main phase of intense magnetic storms, global ENA emissions in the tens of keV energy range exhibit a substantial enhancement in the postmidnight sector. Several important achievements from the IMAGE spacecraft were already documented [e.g., *Burch*, 2003; *Mitchell et al.*, 2003]. In addition, *Burch et al.* [2005] also included some relevant work. A review of ENA imaging technique, history, and future prospect can be found by *C:son Brandt et al.* [2005].

[3] *Lui et al.* [2005] showed for the first time interspacecraft (IMAGE and Geotail) comparison of the energetic neutral oxygen (ENO) intensity in the Earth's magnetosphere during the recovery phase of a magnetic storm on 24–25 November 2001. IMAGE has a high inclination orbit while Geotail has a low one (details are provided in section 3). The energy range of IMAGE/HENA [*Mitchell et al.*, 2000] overlaps with that of the Energetic Particles and Ion Composition (EPIC) instrument on the Geotail spacecraft [*Williams et al.*, 1994], enabling a direct quantitative comparison of ENO intensity from these two instruments. Figure 3 of *Lui et al.* [2005] shows the comparison between the two satellites: the observed ENO fluxes for Geotail/EPIC are significantly higher. A reduction factor of 10 had to be applied to Geotail/EPIC data in order for the energy spectrum to have a good continuity over the combined energy range (as illustrated in Figure 3c of *Lui et al.* [2005]). The intensity differences were verified as not being due to calibration errors of these instruments.

[4] The purpose of this paper is to investigate how different vantage points affect ENA intensity, which is done through the Comprehensive Ring Current Model (CRCM) and ENA simulation. First we want to see whether simulations can reproduce the observational results from IMAGE and Geotail. Then, through comparative analysis of simulation results, we seek to understand the underlying physical parameters/processes for the major differences of the ENO intensity seen by the two spacecraft. The organization of the paper is as follows. Section 2 provides a description of the CRCM and the procedure of obtaining differential ENA fluxes from the modeled ring current ion flux. The orbit

[1]Applied Physics Laboratory, Johns Hopkins University, Laurel, Maryland, USA.
[2]NASA Goddard Space Flight Center, Greenbelt, Maryland, USA.

Copyright 2008 by the American Geophysical Union.
0148-0227/08/2008JA013070

configuration during the event for Geotail and IMAGE is given in section 3. Section 4 shows our simulation results, with section 4.1 describing some specifics on model input and boundary conditions, section 4.2 documenting the reproduction of ENO observations from IMAGE/HENA and Geotail/EPIC, and section 4.3 presenting the role of pitch angle anisotropy in ENO intensity. A discussion and summary of our simulation results and their implications is given in section 5.

2. CRCM and Simulation of ENA

2.1. Comprehensive Ring Current Model

[5] The CRCM [*Fok et al.*, 2001] is a simulation code that self-consistently solves the bounce-averaged Boltzmann convection-diffusion equation of ring current particles and the closure of the currents between the inner magnetosphere and ionosphere. As a combination of the Fok et al. ring current model [e.g., *Fok and Moore*, 1997] and Rice Convection Model (RCM) [*Harel et al.*, 1981; *Toffoletto et al.*, 2003, and references therein], the CRCM has been successful in modeling the storm time ring current behavior as well as the dynamics of the coupled ionosphere [e.g., *Ebihara and Fok*, 2004; *Ebihara et al.*, 2005; *Zheng et al.*, 2006, 2008]. Self-consistency in the electric field is achieved between the ring current particles and the connected ionosphere in the CRCM. Details of the model can be found in the work by *Fok et al.* [2001].

2.2. Simulation of ENA

[6] The CRCM gives ring current ion differential fluxes in time, energy (E), pitch angle (α), and three-dimensional (3-D) spatial location ($\mathbf{r}$). Therefore, the simulated directional differential ENA flux $j_{\mathrm{ENA}}(E)$ (in units of (keV cm^2 s sr)$^{-1}$) at energy E reaching a simulated detector (represented as a 3-D position vector in the simulation) can be calculated by the line of sight (LOS) integration

$$j_{\mathrm{ENA}}(E) = \sum_s \int j_i(\mathbf{r}, E, \alpha) \mathrm{n}_s(\mathbf{r}) \sigma_{\mathrm{is}}(E) \mathrm{dl}, \qquad (1)$$

where $\sigma_{\mathrm{is}}(E)$ is the charge exchange cross section between the energetic ions and the neutrals and $\mathrm{n}_s(\mathbf{r})$ is the geocorona number density. The sum is over all neutral species. The line of sight is determined by the position of the detector. The simulation of ENA from modeled ion fluxes has been applied to studying both terrestrial and planetary environments [*Fok et al.*, 2003, 2004; *Ebihara and Fok*, 2004]. The neutral hydrogen geocorona is described by the spherically symmetric Chamberlain plus exponential model [*Gruntman*, 1997], and the neutral oxygen in the exosphere is described by the MSISE-90 atmospheric model [*Labitzke et al.*, 1985; *Hedin*, 1991]. The pitch angle information is taken into account in the calculation of ENA as shown in equation (1).

[7] Two charge exchange reactions, $O^{+}* + H = O* + H^{+}$ and $O^{+}* + O = O* + O^{+}$, are assumed to dominate in the generation process of the observed energetic neutral oxygen, where the superscript asterisk stands for energetic. Given a spacecraft location, two-dimensional ENA fluxes (a fish-eye view) can be obtained by performing the line of sight integral in (1). The simulated ENA fluxes can then be compared with the measured ENA fluxes captured by an ENA imager, such as IMAGE/HENA.

3. Orbit Configuration and Geophysical Context

[8] To put the simulation results (and their comparison with data) in a better context, Figure 1 illustrates the orbit configuration in geocentric solar magnetic (GSM) coordinates for both IMAGE and Geotail spacecraft. During the period from 1800 UT on 24 November 2001 to 1200 UT on 25 November 2001, Geotail was located in the dayside and moved from (22.14, −14.99, 6.78) R_E to (19.99, −0.71, 4.04) R_E on a nearly equatorial orbit, while IMAGE executed more than one polar orbit. In Figure 1, the asterisk is used to indicate the starting location (at 1800 UT on 24 November 2001) for both spacecraft and the location at 2100 UT on 24 November is marked by a diamond for IMAGE and by a solid circle for Geotail. Figure 2 shows the solar wind and interplanetary magnetic field (IMF) measurements from the ACE spacecraft during the event, along with the *Dst* and *Kp* indices. The quantities from top to bottom are solar wind density, speed, solar wind dynamic pressure, IMF *Bx*, *By*, *Bz*, $|B|$, *Dst* (solid line), and *Kp* (dashed line). The quick look *AU* and *AL* indices are provided by *Lui et al.* [2005], not shown here.

4. Simulation Results

4.1. Model Inputs and Boundary Conditions

[9] To obtain ring current ion fluxes (or, alternatively, the phase space density) from the CRCM, the bounce-averaged drift velocities are calculated using the magnetic field determined by the Tsyganenko 1996 empirical model [*Tsyganenko*, 1995] and the self-consistent electric field by considering the inner magnetosphere and ionosphere coupling. The electric potential at high-latitude boundary (68.4 magnetic latitude) is given by the Hill-Siscoe-Ober Model for the polar cap potential [*Hill et al.*, 1976; *Siscoe et al.*, 2002; *Ober et al.*, 2003]. The model is dependent on solar wind conditions and takes care of the polar cap potential saturation. Also included is the corotation electric field. The height-integrated conductivity in the ionosphere is modeled by including the conductivity caused by solar illumination and that caused by auroral precipitating electrons. The former is calculated using the International Reference Ionosphere (IRI-95) [*Bilitza*, 1997] and the Mass Spectrometer Incoherent Scatter (MSIS-E90) models [*Hedin*, 1991], and the latter is calculated using an empirical model dependent on *Kp* [*Hardy et al.*, 1987]. The flux of protons (H^{+}) at the simulation boundary is assumed to be given by the isotropic Maxwellian distribution with a density of 0.75 cm^{-3} and temperature of 5 keV. Then we divide (as done by *Liemohn et al.* [1999]) the flux between two ion species (H^{+} and O^{+}) using the empirical density ratios found by *Young et al.* [1982], which depend on geomagnetic and solar activity (*Kp* and *F*10.7 indices):

$$\mathrm{O+/H+} = 4.5 \times 10^{-2} \exp(0.17Kp + 0.01F10.7) \qquad (2)$$

$$\mathrm{He+/O+} = 0.013 + 0.015/0.011 \exp(0.24Kp + 0.011F10.7) \qquad (3)$$

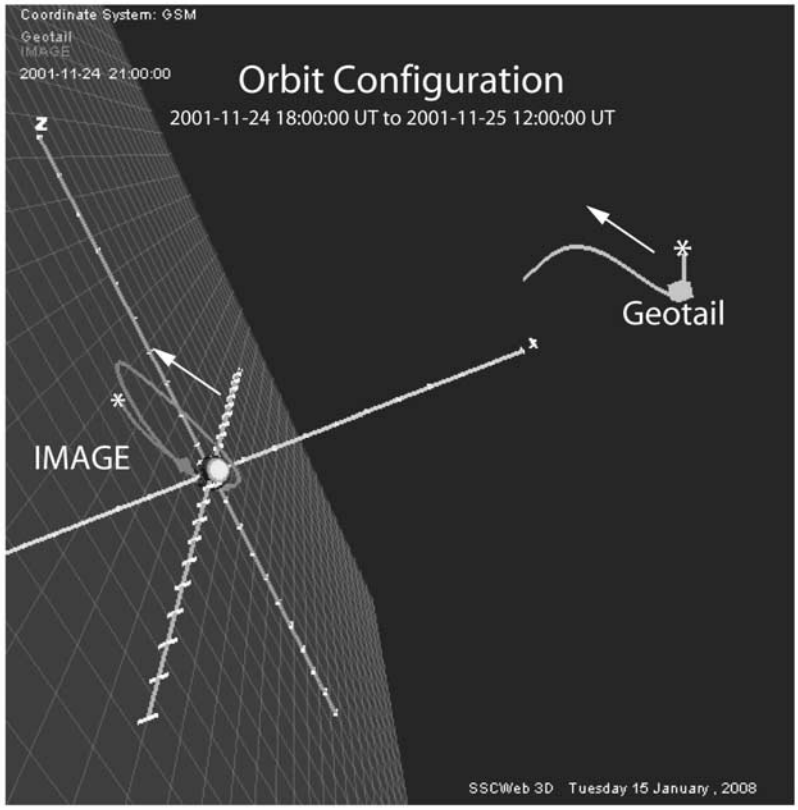

Figure 1. The orbit configuration in GSM coordinates for IMAGE and Geotail spacecraft from 1800 UT on 24 November 2001 to 1200 UT on 25 November 2001. During this interval Geotail was located in the dayside and moved from (22.14, −14.99, 6.78) R_E to (19.99, −0.71, 4.04) R_E on a nearly equatorial orbit while IMAGE executed more than one polar orbit. The asterisk indicates the starting location for both spacecraft, and the location at 2100 UT on 24 November 2001 is marked by a diamond for IMAGE and by a solid circle for Geotail. Figure 1 is made with the assistance from the Satellite Situation Center (SSC) 3-D Orbit Viewer (located at http://sscweb.gsfc.nasa.gov/tipsod/).

He^+ is not considered here as the calculation based on equations (2) and (3) results in ~43.3% O^+ and ~1.7% He^+ heavy ion content at the peak of the storm. The contribution of He^+ to the ring current is, therefore, negligible.

[10] Since the CRCM is driven by solar wind and geomagnetic conditions, we use time-shifted ACE measurements and the measured geomagnetic indices (such as *Dst*, *Kp*, etc.) for our model inputs.

4.2. Simulated ENO Intensity From IMAGE and Geotail

[11] In order to perform a model and data comparison, we first calculate differential oxygen ion fluxes from the CRCM at energies (115, 158, 200, 242, 315, and 422 keV) close to the energy channels of IMAGE/HENA and Geotail/EPIC. Then a two-dimensional fish-eye view of ENO fluxes at any location along the spacecraft trajectory is obtained. The simulation interval is from 0600 UT on 24 November to 1800 UT on 25 November. On the basis of the observations made at the beginning of the simulation (0600 UT on 24 November 2001), the following values are adopted for the T96 model: a solar wind dynamic pressure of 1.81 nPa, a *Dst* value of −9.9 nT, an IMF *By* value of 6.0 nT, and an IMF *Bz* value of −1.3 nT. The magnetic field is kept constant over time. We believe that the choice of the static and quasi quiet time magnetic field model does not significantly affect the model results since our focus is on the recovery phase of a storm.

[12] For a quantitative intercomparison between two spacecraft, a normalization procedure to obtain the total neutral oxygen emission is used. Temporal variations of ENO differential intensities are integrated over a spherical surface encompassing the Earth from both HENA and EPIC, as done by *Lui et al.* [2005]. The procedure is as follows. Given the ENO differential flux at a specific energy channel from pixel i, $J_i(\mathrm{keV} - \mathrm{cm}^2 - \mathrm{s} - \mathrm{sr})^{-1}$, its incident polar angle with respect to the detector surface normal of neutral particles entering that pixel, θ_i, and the solid angle subtended by the pixel, $\Delta\Omega_i$, the total differential intensity from all pixels, $\Psi(\mathrm{keV} - \mathrm{cm}^2 - \mathrm{s})^{-1}$, is then given by $\Psi = \Sigma_i J_i \cos\theta_i \Delta\Omega_i$. With the assumption of isotropic emission, the total intensity integrated over a spherical surface, $\Phi(\mathrm{keV} - \mathrm{s})^{-1}$, is $4\pi r^2\Psi$, where r is the geocentric distance of the satellite.

[13] What we have done is essentially the same as *Jorgensen et al.* [1997] but without the projection (it is unnecessary if the assumption that ENAs measured in each pixel are emitted isotropically is used for mapping). If the total ENA emission intensity from the ring current is I (equivalent as Φ mentioned above), assuming the emission is isotropic, the ENA intensity per area (equivalent to Ψ) is

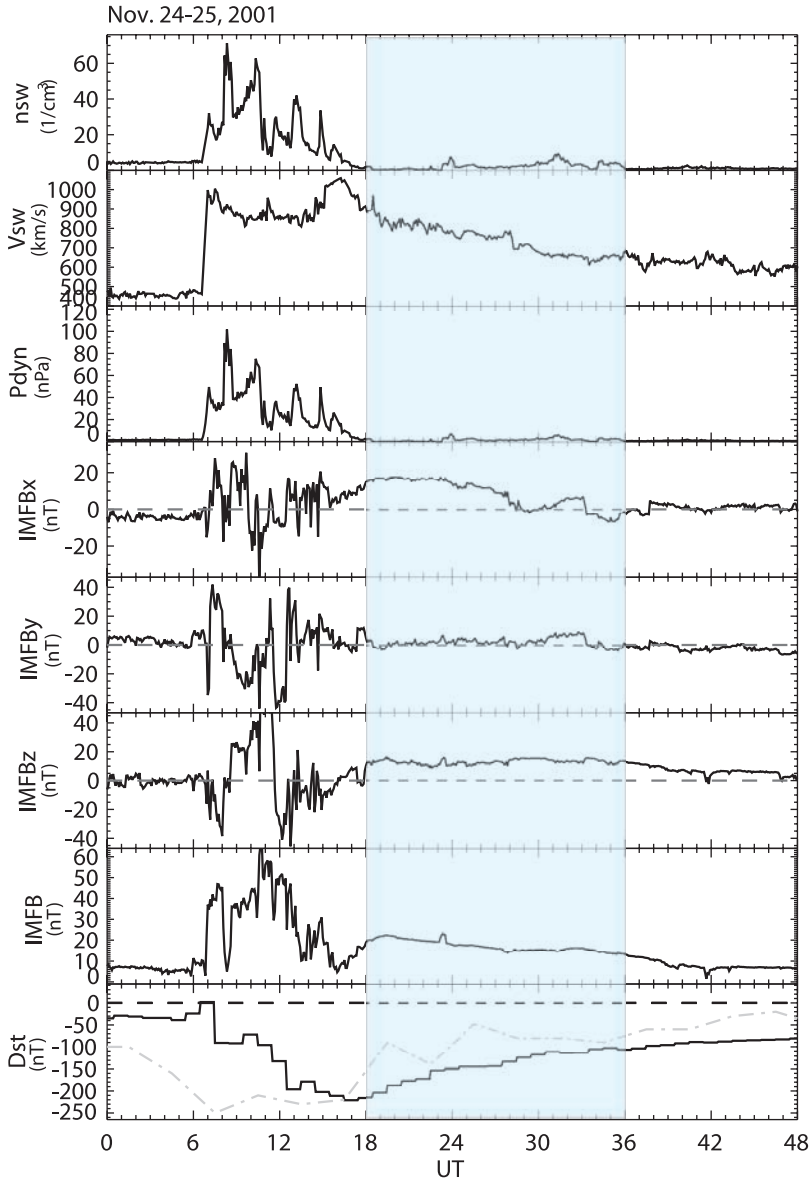

Figure 2. The solar wind/IMF parameters and *Dst* (*Kp*) indices during the 24–25 November 2001 event. The highlighted region is the interval where the ENA observations were made from both spacecraft.

$I/4\pi r^2$. The total intensity is given by $4\pi r^2\Psi$ (=I), which is independent of r as long as r is beyond the ring current region. Since the IMAGE satellite is sometimes inside the ring current region, the calculated total intensity Φ could be less than the actual total intensity but should be only slightly less since the strong ENA emission is very close to Earth. The pitch angle anisotropy information is already captured by $\Psi = \Sigma_i J_i \cos\theta_i \Delta\Omega_i$ through J_i, the differential ENA flux.

[14] Figure 3 shows the temporal variations of the total integrated ENO intensity Φ from both spacecraft on the left (Figure 3a) and the corresponding simulation results on the right (Figure 3b), with the top for IMAGE/HENA and the bottom for Geotail/EPIC. Overplotted in the top of Figure 3b are simulated ENO intensities at 200 and 242 keV (solid line in gray) from Geotail for comparision.

[15] From the observations, for HENA, there was a distinct intensity increase near the end of 24 November followed by a gradual decrease thereafter (top of Figure 3a). This trend of decreasing intensity is consistent with the diminishing storm activity during this recovery phase. For EPIC, the general decrease trend is quite evident. The values from Geotail/EPIC are consistently 1 order of magnitude higher than those from IMAGE/HENA.

[16] Considering the simulation started at 0600 UT on 24 November based on the aforementioned model input and boundary conditions, the simulated neutral oxygen emission intensity has a reasonable agreement with the observations (notice that the scales for observations and simulations are slightly different), such as the intensity at 1800 UT on 24 November for Geotail/EPIC and the general trend of the temporal profile. The simulation results show that the total

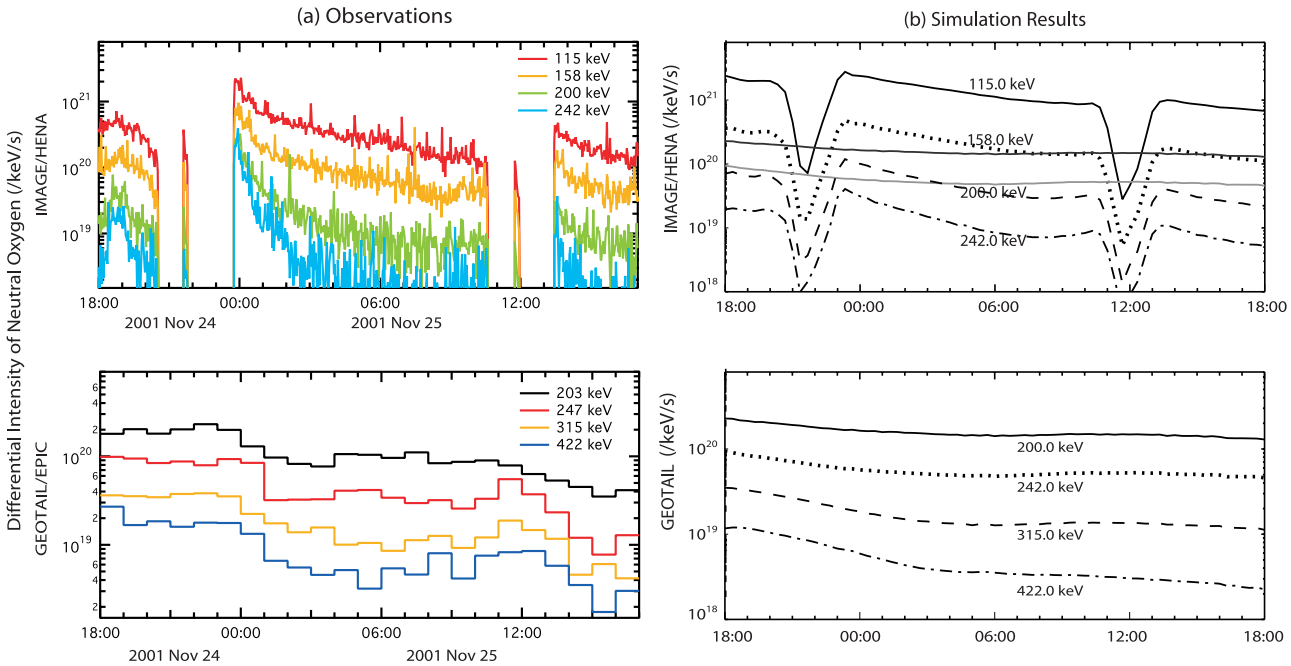

Figure 3. The temporal variations of the total integrated ENO intensity from both spacecraft on the left (Figure 2a) and the corresponding simulation results on the right (Figure 2b), with the top for IMAGE/HENA and the bottom for Geotail/EPIC. Overplotted in the top of Figure 2b are simulated ENO intensities at 200 and 242 keV (solid line in gray) from Geotail for comparision. The time intervals for absence of intensity from IMAGE/HENA in the top of Figure 2a correspond to perigee intervals of IMAGE. Correspondingly, the simulated total neutral intensity (the top of Figure 2b) has a sharp drop during such times as the simulated IMAGE/HENA only "sees" a small part of the total ring current region.

ENO intensities at Geotail are, in general, larger than those from IMAGE (similar to the observation). However, they are less than 1 order of magnitude larger than those of IMAGE/HENA. This may indicate that the actual pitch angle anisotropy is even stronger during the event than that of the simulation. The simulation fails to quantitatively reproduce the decrease of the total neutral oxygen intensity with time, probably because of the lack of complete treatment of energetic oxygen ion loss mechanisms in the model. For example, wave-particle interactions are not included in the simulation. It should be mentioned that the time intervals for absence of intensity from IMAGE/HENA in the top of Figure 3a correspond to perigee intervals of IMAGE. Correspondingly, the simulated total neutral intensity has a sharp decrease during such times as the simulated IMAGE/HENA only "sees" a small part of the total ring current region.

4.3. ENO Intensity Versus Viewing Perspective: Role of Anisotropy

[17] Employing the model inputs that are either based on measurements or within reasonable ranges, our simulation results of the total ENO emission intensity have a good agreement with the observations from Geotail/EPIC and IMAGE/HENA. The simulated ENO intensities from Geotail/EPIC are higher than those from IMAGE/HENA as shown in Figure 3b. These results demonstrate the CRCM's strength in modeling ring current dynamics. However, identifying potential physical causes of the differences in ENO intensity versus viewing perspectives and advancing our understanding through model and data comparison is the ultimate goal of this paper.

[18] Pitch angle anisotropy in plasma fluxes is an important parameter in controlling ring current and radiation belt dynamics, such as wave generation (electromagnetic ion cyclotron waves [e.g., *Kozyra et al.*, 1984; *Engebretson et al.*, 2007] and whistler mode chorus) in the inner magnetosphere and particle precipitation through loss cone loss, etc. With one polar orbiting satellite (IMAGE) and the other one in nearly equatorial orbit (Geotail), pitch angle anisotropy seems to be a natural candidate for explaining the discrepancy in ENO intensity. A dominantly perpendicular distribution of ions (higher flux levels for pitch angles close to $\sim 90°$, mirroring around the equator) will contribute more (large $\cos\theta_i$ at large pitch angles and higher fluxes) to the normalized total intensity Φ viewed by an equatorial vantage point. Vice versa, a dominantly parallel distribution of ions (higher fluxes in small pitch angles, mirroring to high latitudes) will result in a higher total ENA intensity Φ for a polar advantage point. The role of pitch angle anisotropy in leading to different ENO intensities at different viewing perspectives has been verified by our model results. In our simulation run shown in Figure 3b, where Geotail/EPIC saw higher intensities of total ENO emission than IMAGE/HENA, oxygen ions are found to have a perpendicular distribution throughout the 24-h interval. Figure 4 shows the ion distributions at three specific times (1800 UT on 24 November, 0600 UT on 25 November, and

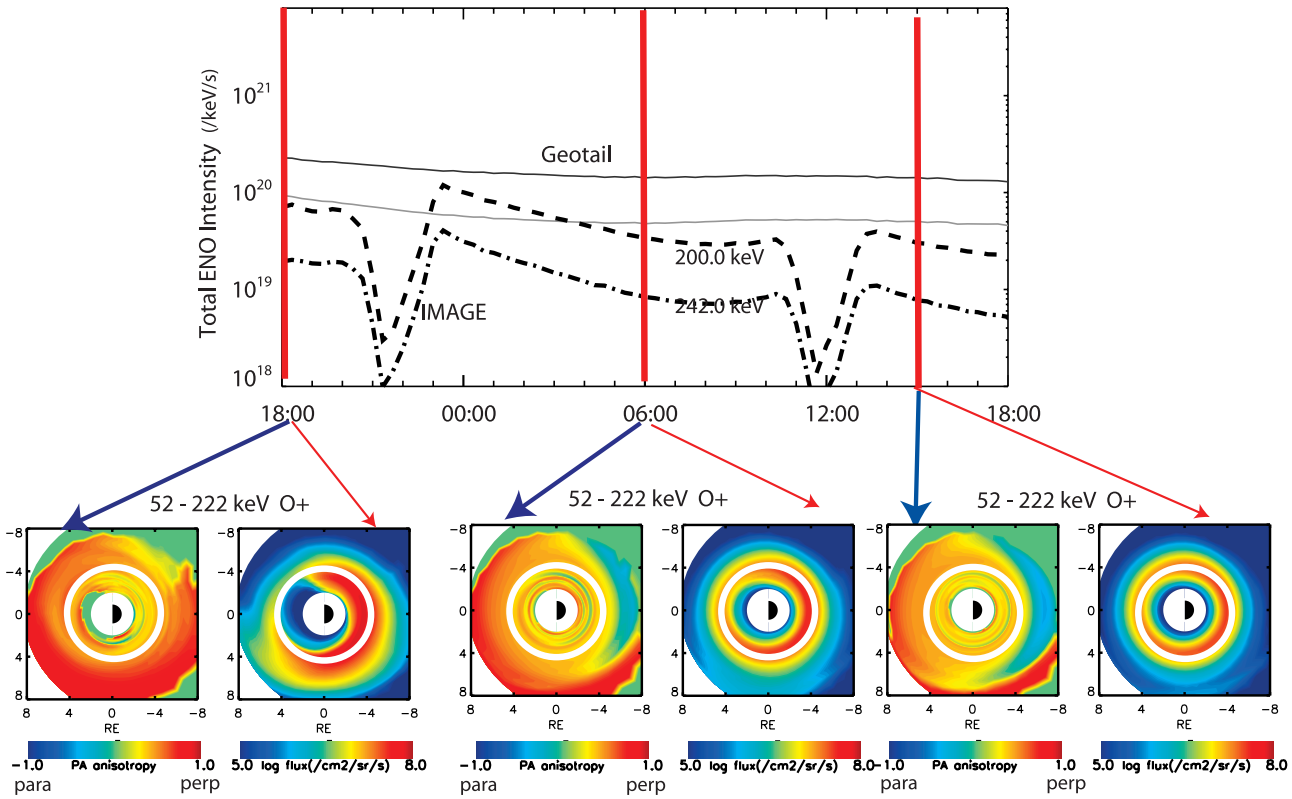

Figure 4. The 52–222 keV O^+ ion distributions at three specific times (1800 UT on 24 November, 0600 UT on 25 November, and 1500 UT on 25 November). The total ENO intensity is provided at the top for reference. For each time, equatorial distributions of (left) pitch angle anisotropy and (right) the logarithmic value of fluxes are shown.

1500 UT on 25 November) with the total ENO intensity shown at the top. For each time, equatorial distributions of both pitch angle anisotropy (on the left, defined as $[F_{perp} - F_{para}][F_{perp} + F_{para}]^{-1}$, where F_{perp} is the perpendicular flux and F_{para} is the parallel flux) for oxygen ions of 52–222 keV and the logarithmic value of fluxes (on the right) are provided. A positive value (red) in pitch angle anisotropy indicates a more perpendicular distribution and vice versa for a parallel distribution (blue). An anisotropy value of zero (green) means the ion distribution is isotropic. The white circles in the plots are used to denote $r = 4\ R_E$.

[19] To further demonstrate the importance of anisotropy to ENO intensity versus viewing perspective, Figure 5 shows simulation results from another run which contrasts with the run in Figures 3 and 4 only in the input values to the T96 model (the other input parameters for the CRCM stay the same). The following values are used in this run for the T96 model: a solar wind dynamic pressure of 5.28 nPa, a *Dst* value of −100 nT, an IMF *By* value of −10 nT, and an IMF *Bz* value of −10 nT. Except for the solar wind dynamic pressure, the other three values are maximal allowable quantities which represent a very stretched magnetic field configuration. In a format similar to Figure 4, the top of Figure 5 shows the simulated total ENO intensities from IMAGE/HENA and Geotail/EPIC at those two overlapping energy channels, with the bottom showing the ion distributions of pitch angle anisotropy and flux at three selected times. We can see that when O^+ has a more perpendicular distribution at 1800 UT on 24 November, the total ENO intensity from Geotail/EPIC is higher; when O^+ has a more parallel distribution at 1500 UT on 25 November, the total ENO intensity from Geotail/EPIC is slightly lower; while at 0600 UT on 25 November, the total ENO intensity from Geotail/EPIC and IMAGE/HENA becomes comparable and, correspondingly, the ion distribution has mixed parallel and perpendicular regions. Figure 5 provides additional evidence of the importance of pitch angle anisotropy and its role in the ENO intensity. The more parallel distribution appearing at the later hours of the interval in Figure 5 results from the stretched magnetic field configuration as the pitch angle of particles at a fixed second adiabatic invariant becomes smaller with the stretching of the field.

5. Discussion and Summary

[20] Our numerical experiments reveal that pitch angle anisotropy could be an important contributor to the ENO intensity difference seen from two perspectives. Conversely, given the difference in the ENO intensity from a polar and an equatorial vantage point, pitch angle anisotropy information can be inferred, with the aid of numerical modeling. Even though our simulation results are performed on O^+ and its ENA intensity due to data availability, the conclusion on the role of pitch angle anisotropy in affecting the total ENA intensity from different viewing angles should also stay true for H^+ ions and corresponding ENAs.

[21] There are advantages and disadvantages associated with different viewing perspectives [*Moore et al.*, 1995].

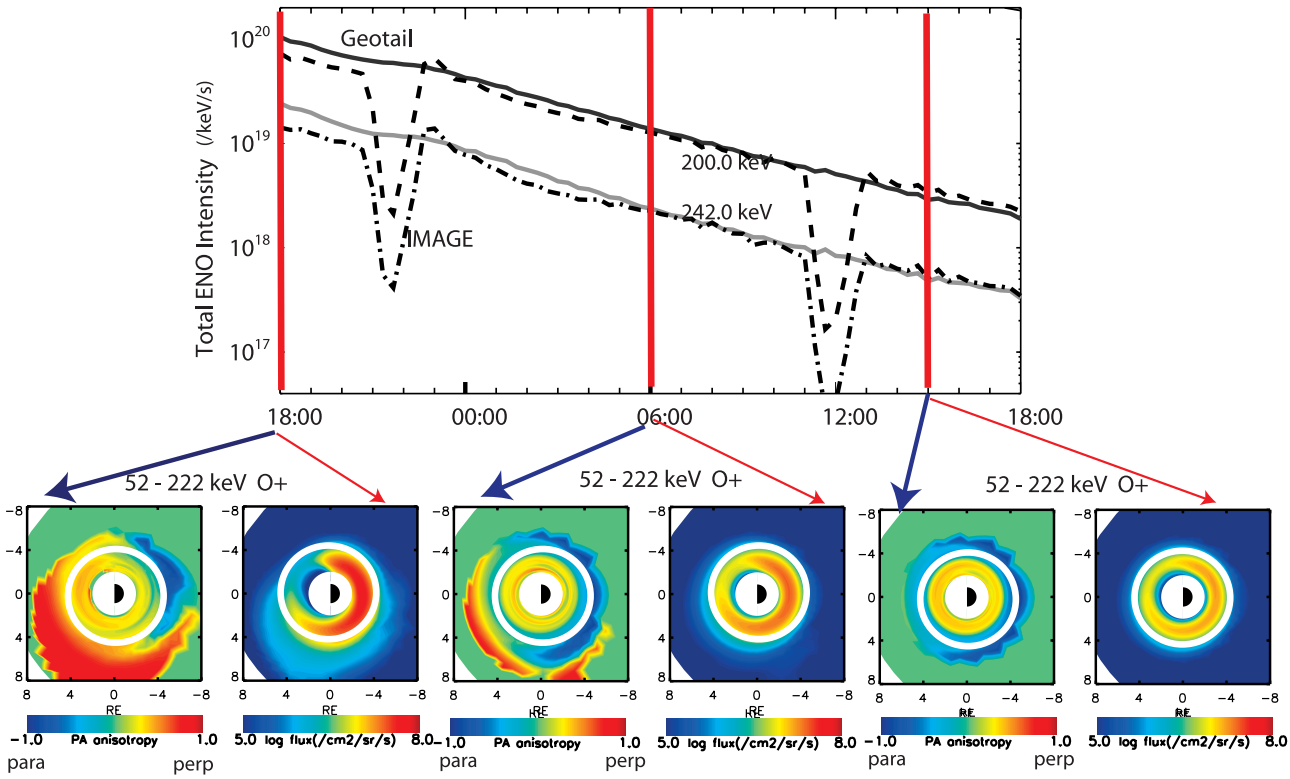

Figure 5. Simulation results from another run in the same format as Figure 3. This run contrasts with the run in Figures 2 and 3 only in the input values to the T96 model. More details are described in the text.

While the ENA image seen from a polar advantage point has good magnetic local time (MLT) resolution of the ring current region (e.g., *C:son Brandt et al.*, 2002, Figure 1), the ENA image resulting from an equatorial vantage point provides a good and direct view of flux tubes and, even more importantly, the information on pitch angle distribution, provided the vantage point is at a proper distance (6–10 R_E, a theoretical optimal range) from the Earth. A vantage point too far away from the Earth (such as Geotail) loses the spatial resolution of its ENA image, and a vantage point too close to the Earth only samples the ENA emissions from a part of the whole ring current region. A good example of this is illustrated in Figure 6 (this is from the simulation result for another different event and is used for making our points).

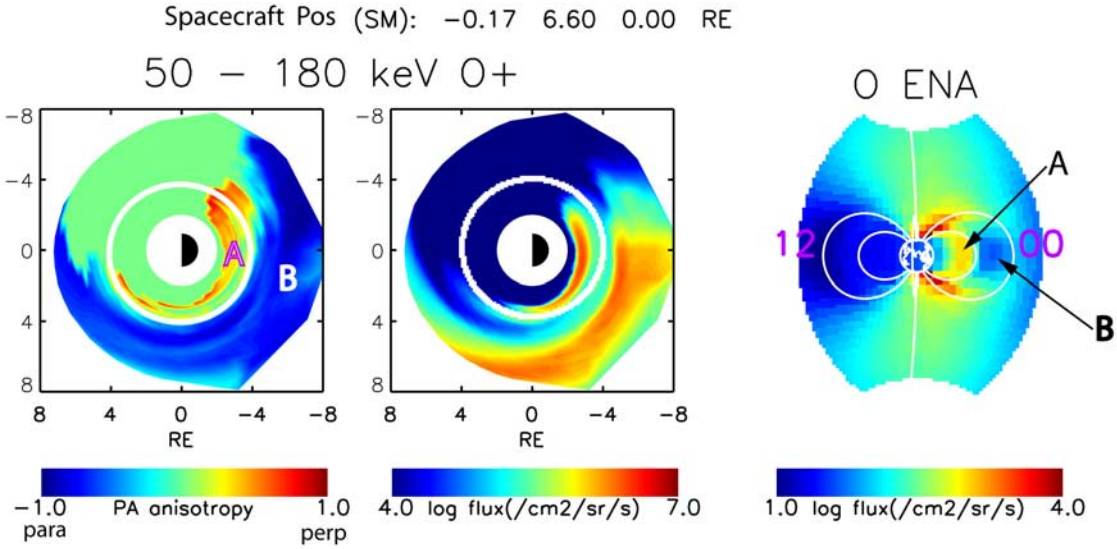

Figure 6. An illustration of advantages of ENA imaging from an equatorial vantage point near 7 R_E.

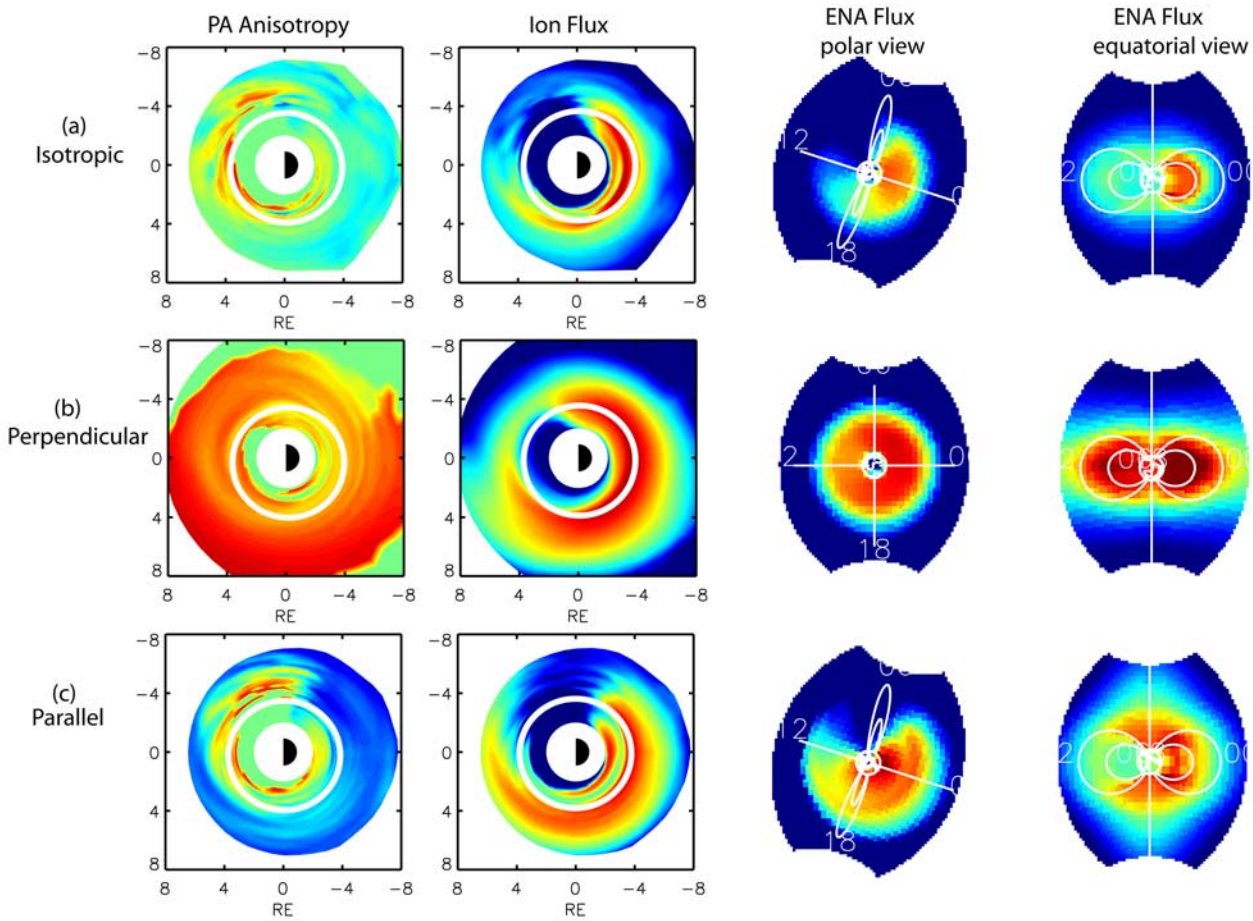

Figure 7. ENA images from both a polar and an equatorial vantage point and their dependence on pitch angle anisotropy, with the intense ring current flux mostly (a) isotropic, (b) perpendicular, and (c) parallel. The first column is the pitch angle anisotropy distribution, the second column is the pitch angle–averaged equatorial ring current flux, the third column is the polar view ENA image (7 R_E from the Earth), and the fourth column is the equatorial view ENA image (7 R_E at dusk).

Figure 6 (left) shows the pitch angle anisotropy distribution of 50–180 keV O^+ at the equator, Figure 6 (middle) is the corresponding equatorial O^+ flux distribution, and Figure 6 (right) is the two-dimensional ENA image seen from a location near the equator at a radial distance of $\sim$7 R_E, with the white lines denoting dipole magnetic field lines at 4 and 8 R_E. From the O^+ flux distribution in the middle, there are two distinct peaks (due to different injections) with the narrow one inside 4 R_E and the broad one farther away from the Earth. The inside flux has a more perpendicular distribution (red, marked by "A" in Figure 6 (left)), while the flux outside 4 R_E exhibits a more parallel distribution (blue, marked by "B" in Figure 6 (left)). Since a perpendicular distribution has higher fluxes at large equatorial pitch angles (higher fluxes for equatorially mirroring particles) and vice versa for parallel distribution (higher fluxes for particles mirroring near the ionospheric foot point of magnetic field lines), a relatively intense ENA emission near the equator is found to be associated with the former (A) while intense ENA emission appears at the ionospheric foot point for the latter (low-altitude emission contributes but with a limited spatial extent). This is shown best from Figure 6 (right), with intense ENA emissions seen inside 4 R_E at the equator and emission minimum farther out. So the equatorial orientated imager can "observe" both ENA intensity along magnetic field lines and at the same time provide anisotropy distribution directly without ENA inversion. Pitch angle anisotropy is still a very poorly measured/understood quantity despite its crucial importance to the generation of waves and to ring current and radiation dynamics. Global ENA imaging, therefore, is a powerful tool of probing inner magnetospheric physics.

[22] A further illustration of the advantages and disadvantages of different viewing perspectives and their dependence on pitch angle anisotropy is provided in Figure 7. ENA images for both polar and equatorial vantage points are shown here for the following three different profiles of the ring current: with the intense ring current flux mostly isotropic in Figure 7a, perpendicular in Figure 7b, and parallel in Figure 7c. The first column is the pitch angle anisotropy distribution, the second column is the pitch angle–averaged equatorial ring current flux, the third column is the polar view ENA image (7 R_E from the Earth), and the fourth column is the equatorial view ENA image (7 R_E at dusk). The color bars are the same for three different cases for easy comparison. The polar view (third column)

provides local time and radial distributions that are convolved with pitch angle information, while the equatorial view reveals well the pitch angle distribution but with the compromise of local time distribution. Simultaneous ENA images from several different vantage points are needed to fully reveal the ring current dynamics. The Two Wide-angle Imaging Neutral-atom Spectrometers (TWINS) mission, using two identical instruments on two widely spaced high-altitude, high-inclination spacecraft, is a step toward that direction. Although the equatorial imaging is demonstrated theoretically to have a big advantage in revealing pitch angle anisotropy of ring current ions, it is technically challenging as the ENA cameras tend to suffer from the penetrating radiation noise.

[23] In summary, our numerical results of ENA intensity show a good agreement with the observations captured by IMAGE/HENA and Geotail/EPIC. The results reveal that pitch angle anisotropy plays an important role in determining ENA intensity from different viewing geometries. Our simulation confirms that global ENA imaging has great potential in unveiling the dynamics of energetic particles by making use of different viewing perspectives. This can contribute greatly to a better understanding of the interconnected inner magnetosphere and ionosphere system.

[24] **Acknowledgments.** The constructive comments from both reviewers are greatly appreciated. We thank all team members of Geotail and IMAGE for making both missions a success. We are grateful to D. G. Mitchell and P. C:son Brandt for the provision of IMAGE/HENA data. We want to acknowledge R. A. Wolf and his coworkers for their contribution in the development of RCM. This work was supported by the NASA grants NNX07AG08G to JHU/APL.

[25] Wolfgang Baumjohann thanks J.-M. Jahn and another reviewer for their assistance in evaluating this paper.

References

Bilitza, D. (1997), International reference ionosphere: Status 1995/96, *Adv. Space Res.*, *20*, 1751–1754, doi:10.1016/S0273-1177(97)00584-X.

Burch, J. L. (2003), The first two years of IMAGE, *Space Sci. Rev.*, *109*, 1–24.

Burch, J. L., M. Schulz, and H. Spence (Eds.) (2005), *Inner Magnetosphere Interactions: New Perspectives From Imaging*, *Geophys. Monogr. Ser.*, vol. 159, 360 pp., AGU, Washington, D.C.

C:son Brandt, P., S. Barabash, E. C. Roelof, and C. J. Chase (2001), ENA imaging at low altitudes from the Swedish microsatellite Astrid: Extraction of the equatorial distribution, *J. Geophys. Res.*, *106*, 25,731–25,744, doi:10.1029/2000JA900023.

C:son Brandt, P., S. Ohtani, D. G. Mitchell, M.-C. Fok, E. C. Roelof, and R. Demajistre (2002), Global ENA observations of the storm mainphase ring current: Implications for skewed electric fields in the inner magnetosphere, *Geophys. Res. Lett.*, *29*(20), 1954, doi:10.1029/2002GL015160.

C:son Brandt, P., D. G. Mitchell, E. C. Roelof, S. M. Krimigis, C. P. Paranicas, B. H. Mauk, J. Saur, and R. DeMajistre (2005), ENA imaging: Seeing the invisible, *Johns Hopkins APL Tech. Dig.*, *26*(2), 143–155.

Ebihara, Y., and M.-C. Fok (2004), Postmidnight storm-time enhancement of tens-of-keV proton flux, *J. Geophys. Res.*, *109*, A12209, doi:10.1029/2004JA010523.

Ebihara, Y., M.-C. Fok, S. Sazykin, M. F. Thomsen, M. R. Hairston, D. S. Evans, F. J. Rich, and M. Ejiri (2005), Ring current and the magnetosphere-ionosphere coupling during the superstorm of 20 November 2003, *J. Geophys. Res.*, *110*, A09S22, doi:10.1029/2004JA010924.

Engebretson, M. J., A. Keiling, K.-H. Fornacon, C. A. Cattell, J. R. Johnson, J. L. Posch, S. R. Quick, K.-H. Glassmeier, G. K. Parks, and H. Rème (2007), Cluster observations of Pc 1–2 waves and associated ion distributions during the October and November 2003 magnetic storms, *Planet. Space Sci.*, *55*, 829–848, doi:10.1016/j.pss.2006.03.015.

Fok, M. C., and T. E. Moore (1997), Ring current modeling in a realistic magnetic field configuration, *Geophys. Res. Lett.*, *24*, 1775–1778, doi:10.1029/97GL01255.

Fok, M.-C., R. A. Wolf, R. W. Spiro, and T. E. Moore (2001), Comprehensive computational model of the Earth's ring current, *J. Geophys. Res.*, *106*, 8417–8424, doi:10.1029/2000JA000235.

Fok, M.-C., et al. (2003), Global ENA IMAGE simulations, *Space Sci. Rev.*, *109*, 77–103, doi:10.1023/B:SPAC.0000007514.56380.fd.

Fok, M.-C., T. E. Moore, M. R. Collier, and T. Tanaka (2004), Neutral atom imaging of solar wind interaction with the Earth and Venus, *J. Geophys. Res.*, *109*, A01206, doi:10.1029/2003JA010094.

Gruntman, M. (1997), Energetic neutral atom imaging of space plasmas, *Rev. Sci. Instrum.*, *68*, 3617, doi:10.1063/1.1148389.

Hardy, D. A., M. S. Gussenhoven, R. Raistrick, and W. J. McNeil (1987), Statistical and functional representations of the pattern of auroral energy flux, number flux, and conductivity, *J. Geophys. Res.*, *92*, 12,275–12,294, doi:10.1029/JA092iA11p12275.

Harel, M., R. A. Wolf, R. W. Spiro, P. H. Reiff, C.-K. Chen, W. J. Burke, F. J. Rich, and M. Smiddy (1981), Quantitative simulation of a magnetospheric substorm: 2. Comparison with observations, *J. Geophys. Res.*, *86*, 2242–2260, doi:10.1029/JA086iA04p02242.

Hedin, A. E. (1991), Extension of the MSIS thermospheric model into the middle and lower atmosphere, *J. Geophys. Res.*, *96*, 1159–1172, doi:10.1029/90JA02125.

Henderson, M., G. Reeves, H. Spence, R. Sheldon, A. Jorgensen, J. Blake, and J. Fennell (1997), First energetic neutral atom images from polar, *Geophys. Res. Lett.*, *24*, 1167–1170, doi:10.1029/97GL01162.

Hill, T., A. Dessler, and R. Wolf (1976), Mercury and Mars: The role of ionospheric conductivity in the acceleration of magnetospheric particles, *Geophys. Res. Lett.*, *3*, 429–432, doi:10.1029/GL003i008p00429.

Jorgensen, A., H. Spence, M. Henderson, G. Reeves, M. Sugiura, and T. Kamei (1997), Global Energetic Neutral Atom (ENA) measurements and their association with the Dst index, *Geophys. Res. Lett.*, *24*, 3173–3176, doi:10.1029/97GL03095.

Kozyra, J. U., T. E. Cravens, A. F. Nagy, and E. G. Fontheim (1984), Effects of energetic heavy ions on electromagnetic ion cyclotron wave generation in the plasmapause region, *J. Geophys. Res.*, *89*, 2217–2233, doi:10.1029/JA089iA04p02217.

Labitzke, K., , J. J. Barnett, and B. Edwards (Eds.) (1985), *Handbook MAP*, vol. 16, Sci. Comm. on Sol.-Terr. Phys., Urbana, Ill.

Liemohn, M., J. Kozyra, V. Jordanova, G. Khazanov, M. Thomsen, and T. Cayton (1999), Analysis of early phase ring current recovery mechanisms during geomagnetic storms, *Geophys. Res. Lett.*, *26*, 2845–2848, doi:10.1029/1999GL900611.

Lui, A. T. Y., D. Williams, E. Roelof, R. McEntire, and D. Mitchell (1996), First composition measurements of energetic neutral atoms, *Geophys. Res. Lett.*, *23*, 2641–2644, doi:10.1029/96GL01194.

Lui, A. T. Y., R. McEntire, M. Nosé, and D. Williams (2001), Composition of energetic neutral atoms during a storm main phase, *Geophys. Res. Lett.*, *28*, 1363–1366, doi:10.1029/2000GL012612.

Lui, A. T. Y. P. C:son Brandt, and D. G. Mitchell (2005), Observations of energetic neutral oxygen by IMAGE/HENA and Geotail/EPIC, *Geophys. Res. Lett.*, *32*, L13104, doi:10.1029/2005GL022851.

Mitchell, D. G., et al. (2000), High energy neutral atom (HENA) imager for the IMAGE mission, *Space Sci. Rev.*, *91*, 67–112, doi:10.1023/A:1005207308094.

Mitchell, D. G., K. Hsieh, C. Curtis, D. Hamilton, H. Voss, E. Roelof, and P. C:son Brandt (2001), Imaging two geomagnetic storms in energetic neutral atoms, *Geophys. Res. Lett.*, *28*, 1151–1154, doi:10.1029/2000GL012395.

Mitchell, D. G., et al. (2003), Global imaging of O^+ from IMAGE/HENA, *Space Sci. Rev.*, *109*, 63–75.

Moore, T. E., M.-C. Fok, J. D. Perez, and J. P. Keady (1995), Evaluating microscale effects on mesoscale transport, in *Cross-scale Coupling in Space Plasmas*, *Geophys. Monogr. Ser.*, vol. 93, edited by J. L. Horwitz et al., p. 37–46, AGU, Washington, D.C.

Ober, D. M., N. C. Maynard, and W. J. Burke (2003), Testing the Hill model of transpolar potential saturation, *J. Geophys. Res.*, *108*(A12), 1467, doi:10.1029/2003JA010154.

Pollock, C., et al. (2001), First medium energy neutral atom (MENA) images of Earth's magnetosphere during substorm and storm-time, *Geophys. Res. Lett.*, *28*, 1147–1150, doi:10.1029/2000GL012641.

Roelof, E. C. (1987), Energetic neutral atom image of a storm-time ring current, *Geophys. Res. Lett.*, *14*, 652–655, doi:10.1029/GL014i006p00652.

Siscoe, G. L., G. M. Erickson, B. U. Ö. Sonnerup, N. C. Maynard, J. A. Schoendorf, K. D. Siebert, D. R. Weimer, W. W. White, and G. R. Wilson (2002), Hill model of transpolar potential saturation: Comparisons with MHD simulations, *J. Geophys. Res.*, *107*(A6), 1075, doi:10.1029/2001JA000109.

Toffoletto, F., S. Sazykin, R. Spiro, and R. Wolf (2003), Inner magnetosphere modeling with the Rice Convection Model, *Space Sci. Rev.*, *107*, 175–196, doi:10.1023/A:1025532008047.

Tsyganenko, N. A. (1995), Modeling the Earth's magnetospheric magnetic field confined within a realistic magnetopause, *J. Geophys. Res.*, *100*, 5599–5612, doi:10.1029/94JA03193.

Williams, D. J., et al. (1994), Geotail energetic particles and ion composition instrument, *J. Geomagn. Geoelectr.*, *46*, 39–57.

Young, D., H. Balsiger, and J. Geiss (1982), Correlations of magnetospheric ion composition with geomagnetic and solar activity, *J. Geophys. Res.*, *87*, 9077–9096, doi:10.1029/JA087iA11p09077.

Zheng, Y., A. T. Y. Lui, M.-C. Fok, B. J. Anderson, P. C:son-Brandt, T. J. Immel, and D. G. Mitchell (2006), Relationship between Region 2 field-aligned current and the ring current: Model results, *J. Geophys. Res.*, *111*, A11S06, doi:10.1029/2006JA011603.

Zheng, Y., P. C:son-Brandt, A. T. Y. Lui, and M.-C. Fok (2008), On ionospheric trough conductance and subauroral ion drift: Simulation results, *J. Geophys. Res.*, *113*, A04209, doi:10.1029/2007JA012532.

M.-C. Fok, NASA Goddard Space Flight Center, Code 673, Greenbelt, MD 20771, USA. (mei-ching.h.fok@nasa.gov)

A. T. Y. Lui and Y. Zheng, Applied Physics Laboratory, Johns Hopkins University, 11100 Johns Hopkins Road, Laurel, MD 20723-6099, USA. (Yihua.Zheng@jhuapl.edu; Tony.lui@jhuapl.edu)